





Cite this: *Energy Adv.*, 2024,  
3, 1710

Received 1st January 2024,  
Accepted 31st May 2024

DOI: 10.1039/d4ya00001c

rsc.li/energy-advances

# Bioinspired flavin analogues as organic electrode materials for supercapacitor applications†

Dipayan Mondal, Ishita Naskar, Melepurath Deepa \* and  
Ashutosh Kumar Mishra \*

With the increasing interest in incorporating redox-active organic molecules as potential materials in energy storage systems, we envisaged a chemical design of a naturally occurring redox-active flavin moiety. Herein, we report the fabrication and characterization of asymmetric supercapacitors (ASCs) based on modified flavins as cathode materials. Notably, subtle chemical modification with the incorporation of a carboxylic functionality around the flavin core (**cFI**) was found to impart superior ion-storage properties compared to a simple flavin derivative (**FI**). As determined, the specific capacitance (SC) for **cFI** and **FI** as individual electrodes was found to be 170 and 62 F g<sup>-1</sup>, respectively, whereas in a two electrode ASC with activated carbon serving as the anode, the SC was found to be 107 and 29 F g<sup>-1</sup>, respectively, at a current density of 1.25 A g<sup>-1</sup>. With better cycling stability (retaining 87% of its initial SC in the case of **cFI**) and significantly higher energy density (38 W h kg<sup>-1</sup> for **cFI**) as compared to most of the known organic material-based electrodes, the modified flavin derivatives serve as better organic electrode alternatives for practical energy storage applications.

## 1. Introduction

Design and development of novel materials for advanced energy storage applications is much needed to cater to the rising demand from electric vehicles, portable electronic products, *etc.*<sup>1</sup> For instance, though supercapacitors are better suited as energy storage devices owing to their high-power densities, long-term cycling stabilities, and faster rechargeability,<sup>2</sup> their lower energy densities severely restrict their widespread usage.<sup>3</sup> Numerous materials have been tried and tested for supercapacitor applications, including nanocarbons,<sup>4</sup> transition metal oxides,<sup>5</sup> and conducting polymers<sup>6</sup> such as polythiophene and polyaniline.<sup>4</sup> However, their energy densities are still about an order of magnitude lower than those of commercial batteries,<sup>7</sup> which fuels the search for novel materials with better energy density, along with durability and fast rechargeability.

Recently, redox-active organic materials owing to their excellent electrochemical reversibility offer an exciting alternative to the existing materials for energy storage applications.<sup>8</sup> Notably, significantly higher specific capacitances (SCs) were reported for these organic materials as compared to porous carbon materials, plausibly due to the multi-electron faradaic reaction

capability of such redox-active organic entities.<sup>9</sup> Interestingly, the incorporation of hetero-atom and/or organic functionalities within the structural framework has been reported to significantly improve the SC, possibly due to the availability of multiple redox sites and increased wettability between the electrode and electrolyte.<sup>10–13</sup> Moreover, structural modulation around the core organic skeleton can be rationally engineered to incorporate multiple active sites resulting in enhanced faradaic redox reactions for better efficiency. Consequently, the demand for novel design strategies for developing suitable redox-active organic molecules as electroactive materials is witnessing a surge.<sup>14,15</sup>

In this context, naturally occurring flavin is known for its redox-active behaviour and is also known to play a pivotal role in various biochemical phenomena, including mitochondrial respiratory chain, signal transduction and DNA repair together with enzymatic chemical transformations.<sup>16–21</sup> Inspired by the redox activities of the flavin entity, modified flavin analogues such as sodium salts of flavin mononucleotides or alloxazine, a tautomeric analogue of isoalloxazine, has recently been investigated as electrolytic materials for the fabrication of redox flow batteries.<sup>22,23</sup> Barring a couple of reports, further modification around the flavin core with the incorporation of suitable functionality to fine-tune the functional behaviour remains largely unexplored.

Interested in designing novel analogues around the flavin core skeleton for various applications such as catalytic transformations, bio-imaging, sensing, and metal coordinated polymers,<sup>24–34</sup> we

Department of Chemistry, Indian Institute of Technology-Hyderabad, Kandi-502284, India. E-mail: akm@chy.iith.ac.in, mdeepa@chy.iith.ac.in

† Electronic supplementary information (ESI) available: The experimental details including synthetic procedure and characterization and photophysical properties. See DOI: <https://doi.org/10.1039/d4ya00001c>

designed and synthesized a novel flavin analogue as an electroactive material for supercapacitor application. The incorporation of carboxyl functionality into the flavin structural framework was envisioned to potentially improve the surface wettability of the electrode and/or enhance ionic conductivity at the electrode–electrolyte interface. The carboxyl functionalized flavin analogue *viz.* 3-(2,4-dioxo-3,4-dihydrobenzo[*g*]pteridin-10(2*H*)-yl) propanoic acid (**cFI**) was synthesized using a slightly modified procedure.<sup>35</sup> A simple flavin without the carboxyl functionality *viz.* 10-propylbenzo[*g*]pteridine-2,4(3*H*, 10*H*)-dione (**FI**) was also used (previously synthesized from our group)<sup>29</sup> as a control to ascertain the role of the carboxyl functionality. In-depth investigations evaluating the electrochemical nature of the synthesized flavin analogues and their applicability for supercapacitors were performed using cyclic voltammetry (CV), galvanostatic charge–discharge (GCD), cycling stability, conductivity, and resistance measurements.

## 2. Result and discussion

### 2.1. Synthesis of flavin analogues

As shown in Scheme 1, the synthesis of **cFI** was achieved by protecting the carboxyl group of  $\beta$ -alanine followed by the nucleophilic aromatic substitution using fluoro-nitrobenzene to give the corresponding nitro derivative **3**. Further reduction of **3** resulted in the monofunctionalized diaminobenzene derivative **4**, which was used without purification for the condensation reaction with alloxan monohydrate in the presence of boric acid in acetic acid/methanol solution to give the isoalloxazine ester derivative **5**. Simple deprotection of the ester derivative resulted in a yield of 85% for our target compound **cFI**. A similar synthetic protocol as reported earlier by our group was used to synthesize **FI**.<sup>29</sup> Standard characterization techniques were used to characterize the final compounds and the details are given in the supporting information section.

### 2.2. Physical characterization

To investigate the morphological topography of the flavin analogues (**cFI** and **FI**), the field emission scanning electron microscopy (FE-SEM) technique was used. Sample preparation involved preparing an aliquot solution containing 0.05 mM **cFI** or **FI** and drop-casting it onto the silicon wafer surface for SEM imaging studies. As shown in Fig. 1A and Fig. S8A (ESI<sup>†</sup>), the SEM micrograph of the **cFI** analogue reveals molten

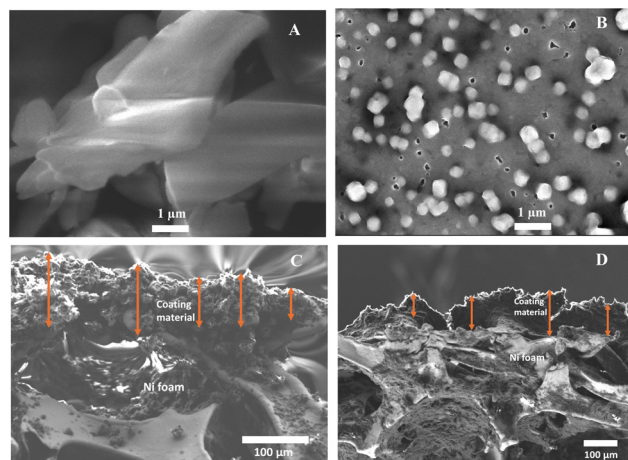


Fig. 1 FE-SEM images of (A) **cFI** and (B) **FI** at 1  $\mu\text{m}$  magnification (concentration of flavins = 0.05 mM). Cross-sectional FE-SEM images of the **cFI**-based electrode material (C) and **FI**-based electrode material (D) at 100  $\mu\text{m}$  magnification.

agglomerates-like textured features with varying shapes and sized particles. Contrarily, the SEM image of **FI** exhibits a completely different morphology with cube-like particles on the silicon wafer surface as shown in Fig. 1B and Fig. S8B (ESI<sup>†</sup>). Further, the thickness of the **cFI** and **FI** based working electrodes was measured and found to be 87.2  $\mu\text{m}$  and 111.6  $\mu\text{m}$ , respectively (Fig. 1C and D).

Further X-ray photoelectron spectroscopy (XPS) studies were performed for **cFI** and **FI** and the data are shown in Fig. 2. The

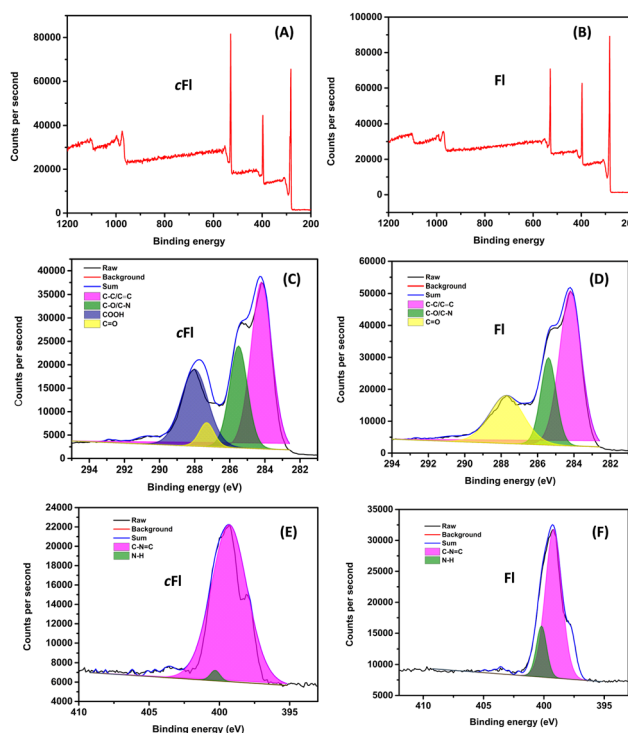
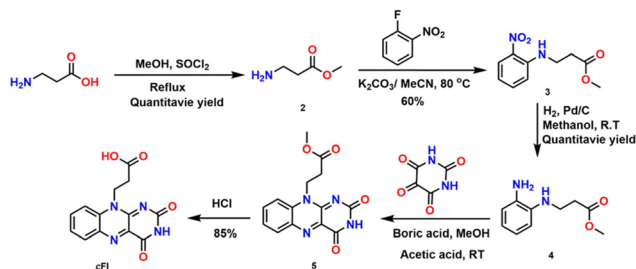


Fig. 2 (A) and (B) XPS core spectra of **cFI** and **FI**. The deconvoluted C 1s (C) and (D) and N 1s (E) and (F) core level spectra of **cFI** and **FI**.



Scheme 1 Schematic representation of the synthesis of **cFI**.

XPS survey spectrum displays the presence of multiple peaks at 282, 397 and 529 eV corresponding to the C 1s, N 1s and O 1s core levels in both the cases. Furthermore, while the deconvoluted C 1s core level spectra of **cFl** and **Fl** display three peaks at 284.2, 285.5, 287.8 and 284.2, 285.2, 287.7 eV, and these peaks correspond to C–C/C=C, C–N/C–O and C=O, respectively, of the isoalloxazine ring common to both compounds. An additional peak in the deconvoluted spectra of **cFl** was observed at 288 eV, which is due to the carboxyl group present in **cFl**. Moreover, the deconvoluted N 1s core level spectrum of **cFl** and **Fl** shows two peaks individually at 399.3, 400.3 and 399.2, 400.2 eV which are attributed to the C–N=C and N–H bonds, respectively.<sup>36</sup>

The composite of **cFl** and carbon black (80:10) was further investigated using N<sub>2</sub> adsorption/desorption isotherms (BET study) and the Barrett–Joyner–Halenda (BJH) analysis to understand the mesoporous nature. As shown in Fig. 3, **cFl** and carbon black composite exhibit a hysteresis loop of type H4 within the typical IV isotherm. Pore size and pore diameter were found to be 17.8091 m<sup>2</sup> g<sup>−1</sup> and 22.55 nm respectively. The carbon black helps in increasing the pore size as well as pore dimensions of **cFl** and carbon black composite.

Further, the BET study and BJH analysis of the individual **cFl** and **Fl** (without mixing carbon black) was also performed. While the **cFl** entity displays a pore size of 5.13 m<sup>2</sup> g<sup>−1</sup> and a pore diameter of 11.27 nm, **Fl** exhibited a pore size of 3.77 m<sup>2</sup> g<sup>−1</sup> and a pore diameter of 12.73 nm. While in general, both the materials exhibit a mesoporous nature with pore dimensions of 2–50 nm, as shown in Fig. S9 (ESI<sup>†</sup>), a subtle difference in the pore size dimension was obtained for **cFl** and **Fl**.

**2.2.1 Redox behaviour of the individual materials (cFl and Fl).** Further efforts were made to understand the electrochemical behaviour of the flavin analogues and possibly to ascertain the significance of incorporated carboxyl functionality at the N10 position of flavin in **cFl**. The initial investigation was performed using a three-electrode setup and the electrochemical behaviour was analysed using CV and GCD techniques. In this study, nickel foam (used as a current collector) was used to coat the working electrodes made from **cFl** and **Fl** materials



Fig. 3 BET plot of **cFl** and the carbon black composite (80:10); inset shows the BJH plot.

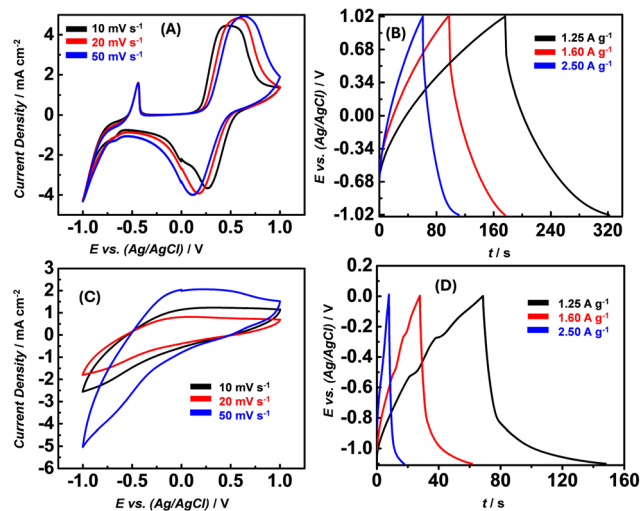


Fig. 4 Electrochemical performances of flavin-based electrodes in the PEO-KOH gel electrolyte in three-electrode systems. (A) Cyclic voltammograms at different scan rates from 10 to 50 mV s<sup>−1</sup> for **cFl**. (B) GCD curves at different current densities from 1.25 to 2.5 A g<sup>−1</sup> for **cFl**. (C) Cyclic voltammograms at different scan rates from 10 to 50 mV s<sup>−1</sup> for **Fl** and (D) GCD curves at different current densities from 1.25 to 2.5 A g<sup>−1</sup> for **Fl**.

(see ESI<sup>†</sup> for details on the electrode fabrication protocol). The electrochemical nature of the flavin analogues in a three-electrode system was evaluated at different scan rates and current densities in the potential window of −1 to +1 V.

The cyclic voltammetry curves for **cFl** and **Fl** recorded at the scan rates of 10, 20 and 50 mV s<sup>−1</sup> are shown in Fig. 4A and C. While for **cFl** the CV curves reveal broad oxidation peaks and comparatively sharper reduction peaks even at all scan rates, almost featureless CV profiles were observed for **Fl**. The observed peaks can be typically assigned to the redox reactions involving the flavin entity. While the peak current remains almost the same with a change in the scan rate, a noticeable shift in the peak potential was observed. With the increase in the scan rate, the cathodic peak was found to shift to the positive side while the anodic peak shifted to the negative side indicative of a diffusion-controlled electron transfer process.

To account for the observed difference in CV plots, although both **cFl** and **Fl** have similar redox cores, CV plots of **cFl** and **Fl** alone were recorded in an aqueous medium (tris buffer, pH = 7.4). As shown in Fig. S13 (ESI<sup>†</sup>), both flavin analogues display similar profiles. Plausibly, the varying interaction due to the presence/absence of carboxyl functionality with that of the PEO-KOH gel electrolyte and/or carbon black and PVdF (polyvinylidene fluoride) used for fabrication purposes might account for the observed difference in the CV profiles.

In addition to the electrochemical characterization, the GCD curves for **cFl** and **Fl** at three different charge/discharge current densities were recorded in the three-electrode configuration. As shown in Fig. 4B and D, the GCD curves for **cFl** and **Fl** display slight deviation from the ideal triangular response with slightly bent curves observed at low voltages during charging and at higher voltages during the discharge process. This observation is suggestive of a shorter charging time needed while a longer

time is required for the discharging process. Interestingly, a sharp difference in the peak shape and size is observed in the GCD curves for **cFl** and **Fl**, displaying a prominent bent curve in the case of **Fl** when compared to that in **cFl**. The comparably longer discharge time in the case of **cFl** indicates slightly better charge storage properties when compared to **Fl**. **Fl** also shows a much larger Ohmic drop compared to **cFl**. This aspect is of paramount importance, especially in view of practical applications, which require a low Ohmic drop.

Further, the specific capacitance (SC) was calculated from the GCD curves using the standard equation ( $SC = I \times \Delta t / m \times \Delta V$ , where  $I$  is the charge–discharge current in Amperes,  $m$  is the mass of the active material in grams, and  $\Delta V$  is the voltage window of operation and  $\Delta t$  is the discharge time in seconds). SCs as determined for **cFl** and **Fl** in the three-electron setups were found to be  $170 \text{ F g}^{-1}$  and  $62 \text{ F g}^{-1}$ , respectively, at a current density of  $1.25 \text{ A g}^{-1}$ . Interestingly, the SC was found to decrease with the increase in the current density as shown with the GCD plot with varying current density (Fig. 4B and D). As determined from the  $C_{sp}$  values calculated at different current densities, the effect seems to be more prominent in the case of **cFl**, as compared to that in **Fl**, with the changes in the  $C_{sp}$  values from  $170$  to  $166 \text{ F g}^{-1}$  and  $62$  to  $15 \text{ F g}^{-1}$ , respectively, when the current density is increased from  $1.25$  to  $2.5 \text{ A g}^{-1}$ . A plausible faradaic reaction of the flavin units in PEO-KOH gel electrolyte is illustrated in Scheme 2, where the isoalloxazine entity undergoes two proton and two electron transfer to attain fully oxidized or fully reduced form.

### 2.2.2 Asymmetric supercapacitors based on **cFl**, and **Fl**.

Further asymmetric supercapacitors (ASCs) were fabricated to evaluate the electrochemical properties of the flavin-based electrode material in a two-electrode configuration setup using activated carbon (AC) as the anodic material and  $1 \text{ M KOH-PEO}$  as the gel electrolyte. The electrochemical performance was analysed by using CV and GCD analysis and the details of cell fabrication are provided in the ESI.† The CV curve of the **cFl**//AC ASC system was recorded in the potential window of  $0$  to  $1.6 \text{ V}$  with varying scan rates (Fig. 5A).

All the CV curves for **cFl**//AC recorded at different scan rates displayed well-defined redox peaks in the anodic and cathodic branches. The slight change in the potential value ( $\Delta E$ ) with the change in the scan rate is indicative of its quasi-reversible nature. Furthermore, the GCD curves recorded in the voltage window of  $0$ – $1.6 \text{ V}$  at different current densities in the range of  $1.25$  to  $2.50 \text{ A g}^{-1}$  as shown in Fig. 5A and B, which reveal comparatively slower current recharge and faster current



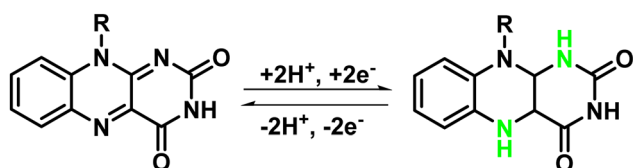
Fig. 5 Electrochemical performances of flavin-based ASCs with a KOH-PEO gel electrolyte: (A) CV plots at different scan rates from  $10$  to  $50 \text{ mV s}^{-1}$  for **cFl**//AC ASC, (B) GCD curves at different current densities from  $1.25$  to  $2.5 \text{ A g}^{-1}$  for **cFl**//AC ASC, (C) CV plots at different scan rates from  $10$  to  $50 \text{ mV s}^{-1}$  for **Fl**//AC ASC and (D) GCD curves at different current densities from  $1.25$  to  $2.5 \text{ A g}^{-1}$  for **Fl**//AC ASC.

discharge with a plateau-like response implying the involvement of faradaic contribution to the charge storage process.

Contrarily, the CV curves for the **Fl**//AC electrode system when recorded at different scan rates in the potential window of  $0$  to  $1.6 \text{ V}$ , display quasi-leaf-like shapes with a broad oxidation peak and broad reduction wave, indicative of charge storage being dominated by the electrical double layer (EDL) formation. Furthermore, the GCD curves recorded at different current densities in the range of  $1.25$  to  $2.50 \text{ A g}^{-1}$  further corroborate the observed CV curves with a moderately curved potential decay profile, over the  $1.6 \text{ V}$  potential domain, as shown in Fig. 5C and D. Both these observations are suggestive of the underlying EDLC process for charge storage at the electrode–electrolyte interface.<sup>37</sup>

Further, SC was calculated using the method mentioned above from the GCD curves at the different current densities ranging from  $1.25$  to  $2.5 \text{ A g}^{-1}$ . Interestingly, **cFl**//AC ASC delivered higher SC values of ( $107$  to  $103 \text{ F g}^{-1}$ ) as compared to much lower values of ( $29$ – $22 \text{ F g}^{-1}$ ) for **Fl**//AC ASC. A similar observation was made in the case of the electrode system. The proposed structural variation in **cFl** compared to **Fl** seems to play an important role in deciding the capacitance properties. While the major redox behaviour can be attributed to the core flavin entity, the presence of carboxylic functionality in the case of **cFl**, possibly decreases the electrode surface resistivity as well as increases the surface wettability for the physisorption of the electrolytic ions on the electrode, thereby enhancing the ionic conductivity at the electrode–electrolyte interfaces.<sup>37</sup>

Additionally, the linear sweep voltammetry (LSV) plots were recorded to evaluate the electrochemical stability window of the **cFl** and **Fl** electrode materials and are shown in Fig. 6A. A potential range of  $-2 \text{ V}$  to  $+2 \text{ V}$  and a scan rate of  $10 \text{ mV s}^{-1}$  at  $25^\circ \text{C}$ , were used for the measurements and the slopes of the resulting  $I$ – $V$  curves



Scheme 2 Faradaic reaction of flavin units in PEO-KOH gel solution.







Fig. 6 (A) Linear sweep voltammetry (LSV) curves of **cFI**//AC and **FI**//AC ASCs at a scan rate of  $10 \text{ mV s}^{-1}$  (B) Nyquist plots for **cFI**//AC and **FI**//AC ASCs, (C) electrochemical cycling performance of **cFI**//AC and **FI**//AC ASCs over 10 000 cycles at a current density of  $4 \text{ A g}^{-1}$  and (D) Ragone plots for **cFI**//AC and **FI**//AC ASCs.

gave the electrical conductance of **cFI**- and **FI**-based electrodes directly, and the values were found to be  $170$  and  $0.8 \text{ mS cm}^{-1}$ , respectively.

Electrochemical impedance spectra were recorded to further understand the charge transfer and transport behaviour of the **cFI**//AC and **FI**//AC ASCs. As shown in Fig. 6B, an AC bias of  $20 \text{ mV}$  was applied over a frequency range of  $1 \text{ MHz}$  to  $0.01 \text{ Hz}$ , and the data were fitted into the  $[R(RC)W]$  circuit. The fitted parameters are summarized in Table 1. As shown in Fig. 6B, the Nyquist plots for **cFI** and **FI**-based electrodes display a straight line with a linear rise in the low-frequency region in the case of **cFI**, which is indicative of significant capacitive behaviour with low diffusion resistance. Contrarily, the **FI**-based electrode displayed a skewed semicircle followed by an inclined line, indicating a higher equivalent series resistance and a lower capacitive behaviour. Also, the charge transfer resistance ( $R_{ct}$ ) was found to be lower for **cFI**//AC ( $1.40 \text{ } \Omega \text{ cm}^2$ ) as compared to that for **FI**//AC ( $11.69 \text{ } \Omega \text{ cm}^2$ ) ASCs. This observation further supports that the cation and anion accumulation from the KOH-PEO gel electrolyte at the electroactive sites of the **cFI**-based electrode are more facile when compared to the **FI**-based electrode.

Furthermore, to ascertain the stability of **cFI** and **FI** electrode materials for their practical usage as electrochemical supercapacitors, the cycling stabilities of **cFI**//AC and **FI**//AC were investigated at a current density of  $5 \text{ A g}^{-1}$  for 2500 cycles.

Table 1 Fitted impedance parameters for the two ASCs with a KOH-PEO gel

| Device          | $R_s$ ( $\Omega \text{ cm}^2$ ) | $R_{ct}$ ( $\Omega \text{ cm}^2$ ) | $C_{dl}$ ( $\text{F cm}^{-2}$ ) |
|-----------------|---------------------------------|------------------------------------|---------------------------------|
| <b>cFI</b> //AC | 0.40                            | 1.40                               | $1.1 \times 10^{-3}$            |
| <b>FI</b> //AC  | 0.23                            | 11.69                              | $2.8 \times 10^{-4}$            |

Interestingly, a clear distinction between the **cFI**//AC-based ASCs was observed, where **cFI** as the electrode displayed excellent electrochemical stability retaining about 94% of its initial SC as compared to the 71% retention capability displayed by the **FI**//AC ASC (Fig. S10, ESI†). Furthermore, the number of cycles was increased to 10 000 cycles for both materials to observe the loss of cycling performance. Notably, only a 7% loss of cycling performance was observed for **cFI** (cycling stability = 87%), whereas a 5% loss of cycling performance was observed for **FI** (cycling stability = 66%) (Fig. 6C), when compared to the cycling stability after 2500 cycles. The observed cycling stability for **cFI**-based ASC was observed to be among the best of the organic molecule-based electrode materials with close to 90% retention capability after 10 000 cycles.<sup>38</sup>

Furthermore, the Ragone plots were plotted for **cFI**//AC and **FI**//AC ASCs to evaluate the energy and power densities of the cells. As shown in Fig. 6D, the power density versus energy density plot for **cFI** and **FI**-based ASCs, the maximum energy density was found to be  $\sim 38 \text{ W h kg}^{-1}$ , for the **cFI**-based system while the comparably lower energy density of  $\sim 10 \text{ W h kg}^{-1}$  was observed in the case of **FI**-based ASC at a given power density of  $1 \text{ kW kg}^{-1}$ . Notably, the energy density of  $\sim 34 \text{ W h kg}^{-1}$  was retained for **cFI**//AC ASC as compared to  $\sim 7 \text{ W h kg}^{-1}$  for **FI**//AC ASC when the power density was increased to  $2.6 \text{ kW kg}^{-1}$ .

To further determine the electrochemical process and capacitive and diffusive components of **cFI**//AC, the following equations were used.

$$i(V) = i_{cap} + i_{diff} = k_1 v + k_2 v^{1/2}$$

or,

$$i(V)/v^{1/2} = k_1 v^{1/2} + k_2$$

$i_{cap}$  and  $i_{diff}$  are the capacitive and diffusive current contributions respectively.

The capacitive and diffusive contributions for the **cFI**//AC electrode in percentages are shown in Fig. 7A. The advantage of the capacitive effect is more significant when the scan rate changes from higher to lower values, with 91% of capacitive and 9% of diffusive contributions at  $10 \text{ mV s}^{-1}$ . The effect of the capacitance control gradually decreases when the scanning rate increases, and the proportion of ion diffusion control increases. The CV plot illustrating the total contribution



Fig. 7 (A) Capacitive and diffusion control percentage with different scan rates of the **cFI**//AC electrode. (B) Proportion of surface control at  $10 \text{ mV s}^{-1}$ .



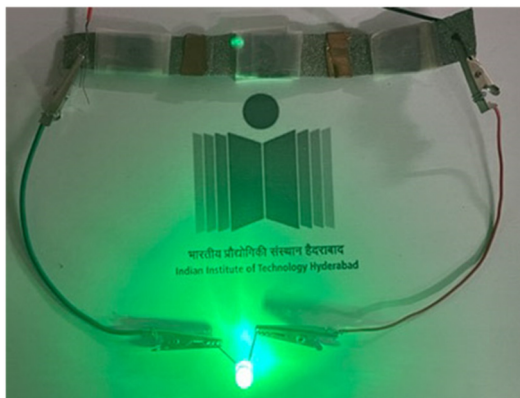


Fig. 8 Photographs of the green LED bulb being lit up using three cFI-based ASCs connected in a series.

(diffusive and capacitive) and the diffusive contribution in the shaded curve are shown in Fig. 7B. The constants  $k_1$  and  $k_2$  were calculated from the slope and the intercept of a linear plot of  $i(V)/\nu^{1/2}$  versus  $\nu^{1/2}$ .

Notably, much better electrochemical performance was reported with transition metals oxides/sulfides-based electrode materials when compared with the cFI-based material.<sup>39–45</sup> However, the cFI-based material demonstrates a comparable result with reported organic-based supercapacitors. A comparison of energy density value for the cFI//AC with the reported organic supercapacitor-based electrodes is given in Table S1 (ESI†).<sup>46–52</sup>

Furthermore, to verify the practicability of the cFI electrode material for its practical behavior, three cFI-based asymmetrical ASC cells were connected in a series. The fully charged 3S assembly consisting of the cFI-based electrodes was observed to illuminate a green light emitting diode (LED) for approximately 35 s; thereby supporting the usage of the flavin-based material for ASCs (Fig. 8).

### 3. Conclusions

In conclusion, molecular design around the naturally occurring redox-active flavin core skeleton was envisaged, synthesized, and evaluated for energy storage applications. Subtle chemical modification incorporating a carboxyl functionality within the flavin core (cFI) was synthesized and compared with a simple flavin (FI) analogue as efficient electrode material. As observed, significant variation in the electrochemical behavior was observed between the two flavin analogues as electrodes with comparably better efficiency in the case of cFI. In a three-electrode setup, SCs of  $170 \text{ F g}^{-1}$  and  $62 \text{ F g}^{-1}$  were achieved for cFI and FI, respectively, at a current density of  $1.25 \text{ A g}^{-1}$ . The practical applicability of the flavin as electrode materials was evaluated by fabricating cFI//AC and FI//AC ASCs and KOH-PEO gel electrolytes, which revealed the SC of  $107 \text{ F g}^{-1}$  and  $29 \text{ F g}^{-1}$ , respectively. In addition, better cyclic stability was observed for cFI (87% retention), while the energy densities of  $38 \text{ W h kg}^{-1}$  in the case of cFI and  $10 \text{ W h kg}^{-1}$  in the case of FI

were obtained at a power density of  $1 \text{ kW kg}^{-1}$ . Moreover, impedance and LSV analysis further support the chemically modified flavin analogue cFI-based electrode material as a potential candidate for energy storage devices.

### Conflicts of interest

There are no conflicts to declare.

### Acknowledgements

D. M. thanks PMRF (MHRD) for the scholarship. I. N. thankful to CSIR-India for a scholarship. A. K. M. thanks SERB India for the (CRG/2022/006706), for the research funding. All authors thank the Indian Institute of Technology (IIT)-Hyderabad for providing infrastructure and instrument facilities.

### References

- 1 C. Liu, F. Li, L. P. Ma and H. M. Cheng, *Adv. Mater.*, 2010, **22**, E28–E62.
- 2 C. Zhong, Y. Deng, W. Hu, J. Qiao, L. Zhang and J. Zhang, *Chem. Soc. Rev.*, 2015, **44**, 7484–7539.
- 3 J. Armenta, C. Núñez, N. Visair and I. Lázaro, *J. Power Sources*, 2015, **284**, 452–458.
- 4 S. Saha, P. Samanta, N. C. Murmu and T. Kuila, *J. Energy Storage*, 2018, **17**, 181–202.
- 5 *Nanomaterials in Advanced Batteries and Supercapacitors, Transition metal oxides as supercapacitor materials*, ed K. I. Ozoemena and S. Chen, Springer, New York, 2016, 317–344.
- 6 Q. Meng, K. Cai, Y. Chen and L. Chen, *Nano Energy*, 2017, **36**, 268–285.
- 7 P. Simon and Y. Gogotsi, *Nat. Mater.*, 2008, **7**, 845–854.
- 8 P. Poizot, J. Gaubicher, S. Renault, L. Dubois, Y. Liang and Y. Yao, *Chem. Rev.*, 2020, **120**, 6490–6557.
- 9 T. R. Kuo, L. Y. Lin, S. Kubendhiran, Y. C. Li, R. J. Chung and S. Yougbaré, *J. Energy Storage*, 2022, **53**, 105085.
- 10 C. Largeot, C. Portet, J. Chmiola, P. L. Taberna, Y. Gogotsi and P. Simon, *J. Am. Chem. Soc.*, 2008, **130**, 2730–2731.
- 11 L. Z. Fan, S. Qiao, W. Song, M. Wu, X. He and X. Qu, *Electrochim. Acta*, 2013, **105**, 299–304.
- 12 X. Ma, W. Zhou, D. Mo, J. Hou and J. Xu, *Electrochim. Acta*, 2015, **176**, 1302–1312.
- 13 M. D. Najafi, E. Kowsari, H. R. Naderi, A. Chinnappan, S. Ramakrishna, A. Ehsani and A. Shokravi, *Compos. Sci. Technol.*, 2021, **211**, 108844.
- 14 X. Chen, X. Feng, B. Ren, L. Jiang, H. Shu, X. Yang, Z. Chen, X. Sun, E. Liu and P. Gao, *Nano-Micro Lett.*, 2021, **13**, 1–6.
- 15 F. Ma, X. Wang, Z. Hu, L. Hou, Y. Yang, Z. Li, Y. He and H. Zhu, *Energy Fuels*, 2020, **34**, 13079–13088.
- 16 A. M. Edwards, *Methods Mol. Biol.*, 2014, **1146**, 3–13.
- 17 S. Ghisla and D. E. Edmondson, *Flavin Coenzymes*, John Wiley & Sons, Ltd, Hoboken, NJ, 2001, pp. 1–9.
- 18 A. Sancar, *Chem. Rev.*, 2003, **103**, 2203–2238.



- 19 I. Chaves, R. Pokorny, M. Byrdin, N. Hoang, T. Ritz, K. Essen, L. O. Brettel, G. T. van der Horst, A. Batschauer and M. Ahmad, *Annu. Rev. Plant Biol.*, 2011, **62**, 327–364.
- 20 A. Lukacs, P. J. Tonge and S. R. Meech, *Acc. Chem. Res.*, 2022, **55**, 402–414.
- 21 T. E. Swartz, S. B. Corchnoy, J. M. Christie, J. W. Lewis, I. Szundi, W. R. Briggs and R. A. Bogomolni, *J. Biol. Chem.*, 2001, **276**, 36493–36500.
- 22 A. Orita, M. G. Verde, M. Sakai and Y. S. Meng, *Nat. Commun.*, 2016, **7**, 1–8.
- 23 K. Lin, R. Gómez-Bombarelli, E. S. Beh, L. Tong, Q. Chen, A. Valle, A. Aspuru-Guzik, M. J. Aziz and R. G. Gordon, *Nat. Energy*, 2016, **1**, 1–8.
- 24 M. V. Mouli, D. Mondal, K. Kumari, S. K. Singh and A. K. Mishra, *Org. Biomol. Chem.*, 2023, **21**, 3311–3316.
- 25 M. V. Mouli, S. Katyal and A. K. Mishra, *Synlett*, 2023, 829–834.
- 26 M. V. Mouli and A. K. Mishra, *RSC Adv.*, 2022, **12**, 3990–3995.
- 27 M. V. Mouli and A. K. Mishra, *Dyes Pigm.*, 2023, **121**, 111148.
- 28 M. V. Mouli and A. K. Mishra, *Org. Biomol. Chem.*, 2023, **21**, 5622–5628.
- 29 M. V. Mouli and A. K. Mishra, *CrystEngComm*, 2022, **24**, 2221–2225.
- 30 M. V. Mouli, H. G. Agrawal, T. Maddeshiya, A. Tamrakar, S. R. Tripathy, M. D. Pandey and A. K. Mishra, *Luminescence*, 2023, **38**, 1206–1214.
- 31 M. V. Mouli, H. G. Agrawal, M. Kumar and A. K. Mishra, *Luminescence*, 2023, **38**, 1185–1191.
- 32 M. V. Mouli and A. K. Mishra, *ChemistrySelect*, 2022, **7**, e202202126.
- 33 H. G. Agrawal, S. Khatun, A. K. Rengan and A. K. Mishra, *Polyhedron*, 2023, **243**, 116536.
- 34 H. G. Agrawal, P. S. Giri, P. Meena, S. N. Rath and A. K. Mishra, *ACS Med. Chem. Lett.*, 2023, **14**(12), 1857–1862.
- 35 M. V. Mouli and A. K. Mishra, *J. Chem. Sci.*, 2022, **134**, 59.
- 36 F. Ma, Z. Hu, L. Jiao, X. Wang, Y. He, Y. Yang and Z. Li, *ACS Appl. Energy Mater.*, 2021, **4**, 5493–5503.
- 37 J. Shen, A. Liu, Y. Tu, G. Foo, C. Yeo, M. B. Chan-Park, R. Jiang and Y. Chen, *Energy Environ. Sci.*, 2011, **4**, 4220–4229.
- 38 N. An, Z. Hu, H. Wu, Y. Yang, Z. Lei and W. Dong, *J. Mater. Chem. A*, 2017, **5**, 25420–25430.
- 39 H. Y. Jung, S. I. Kim, J. Kim, Y. J. Kim, H. Hong, J. Yun and W. Ryu, *J. Mater. Chem. A*, 2023, **11**, 20608–20622.
- 40 T. Zhu, Z. He, Z. An, R. Xu, Y. Li, R. Zhe, H. E. Wang and H. Pang, *Sci. China Mater.*, 2023, **66**, 2216–2226.
- 41 P. S. Chauhan, S. Kumar, A. Mondal, P. Sharma, M. N. Parekh, V. Panwar, A. M. Rao and A. Misra, *J. Mater. Chem. A*, 2023, **11**, 95–107.
- 42 T. Zhu, J. Pan, Z. An, R. Zhe, Q. Ou and H. E. Wang, *J. Mater. Chem. A*, 2022, **10**, 20375–20385.
- 43 Y. Zang, H. Luo, H. Zhang and H. Xue, *ACS Appl. Energy Mater.*, 2021, **4**, 1189–1198.
- 44 Y. Ren, T. Zhu, Y. Liu, Q. Liu and Q. Yan, *Small*, 2021, **17**, 2008047.
- 45 S. Thareja and A. Kumar, *ACS Sustainable Chem. Eng.*, 2021, **9**, 2338–2347.
- 46 L. Jiao, Z. Hu, F. Ma, Y. He, Q. Zhou, L. Xiao, L. Lv and Y. Yang, *J. Energy Storage*, 2022, **52**, 104777.
- 47 F. Ma, Z. Hu, L. Jiao, X. Wang, Y. He, Y. Yang and Z. Li, *ACS Appl. Energy Mater.*, 2021, **4**, 5493–5503.
- 48 H. Peng, R. Zhao, J. Liang, S. Wang, F. Wang, J. Zhou, G. Ma and Z. Lei, *ACS Appl. Mater. Interfaces*, 2018, **10**, 37125.
- 49 F. Ma, Z. Hu, L. Jiao, X. Wang, Y. Yang, Z. Li and Y. He, *Adv. Mater. Interfaces*, 2021, **8**, 2002161.
- 50 F. Ma, X. Wang, Z. Hu, L. Hou, Y. Yang, Z. Li, Y. He and H. Zhu, *Energ Fuel*, 2020, **34**, 13079–13088.
- 51 G. Lv, X. Dai, Y. Qiao, G. Ren, H. Fan, Y. Liu and Y. Chen, *J. Chem. Eng.*, 2023, **470**, 144068.
- 52 Z. Song, D. Zhu, L. Li, T. Chen, H. Duan, Z. Wang, Y. Lv, W. Xiong, M. Liu and L. Gan, *J. Mater. Chem. A*, 2019, **7**, 1177–1186.

